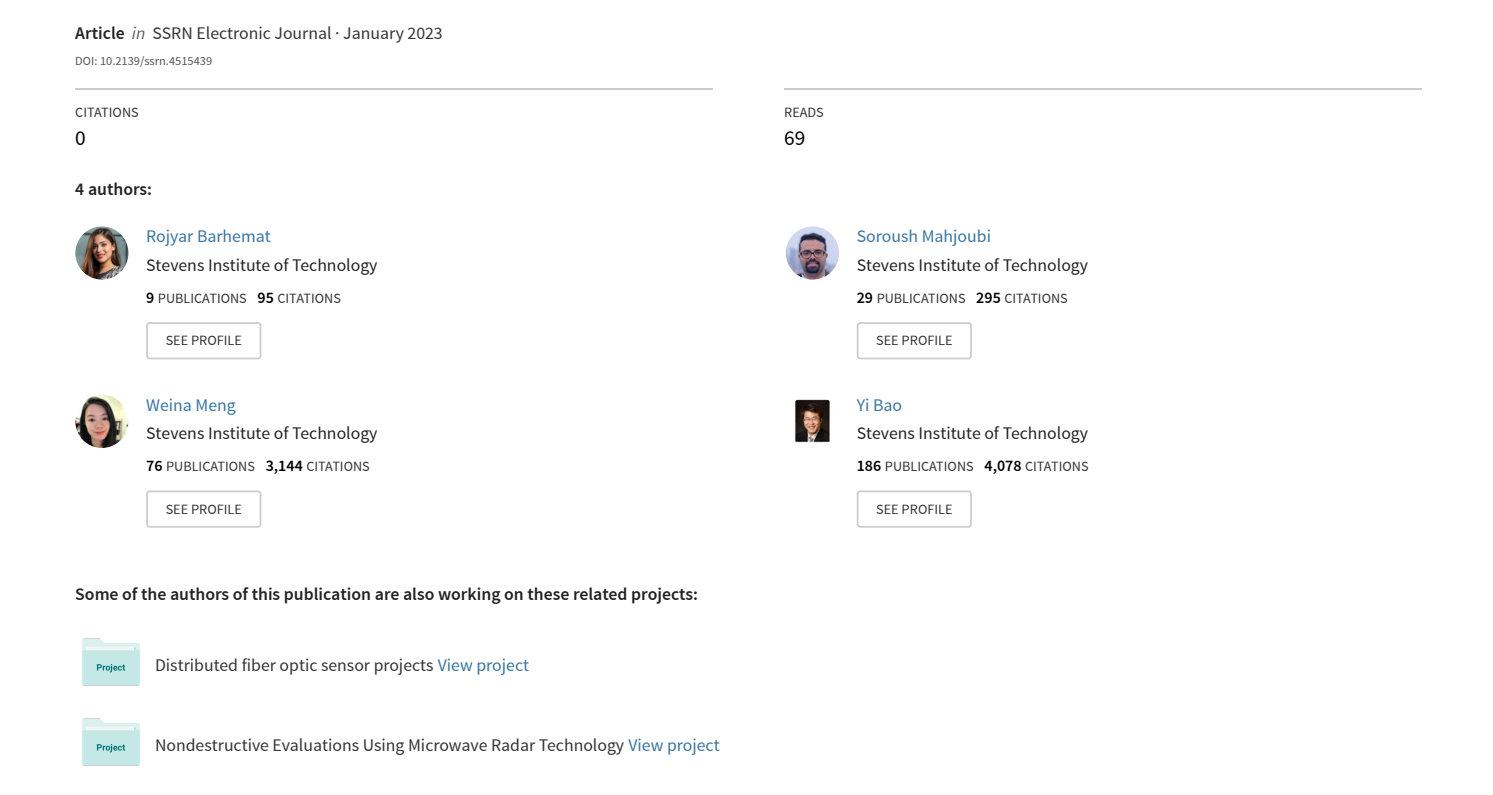
# AI-assisted Design, 3d Printing, and Evaluation of Architecture Polymerconcrete Composites (APCC) With High Specific Flexural Strength and High Specific Toughness



- AI-assisted design, 3D printing, and evaluation of architectured polymer-concrete 1 2 composites (APCC) with high specific flexural strength and high specific toughness Rojyar Barhemat, Soroush Mahjoubi, Weina Meng, Yi Bao \* 3 Department of Civil, Environmental and Ocean Engineering, Stevens Institute of Technology, 4 5 Hoboken, New Jersey 07030, USA \* Corresponding author: vi.bao@stevens.edu 6 7 **Abstract** Architectured polymer-concrete composite (APCC) is a promising structural material with 8 9 high mechanical performance. Optimizing the design of APCC for a high flexural strength, high toughness, and light weight remains a challenge. This paper presents a machine learning-based 10 11 optimization framework to design APCC with high specific flexural strength and high toughness. 12 The proposed framework integrates sequential surrogate modelling, Latin hypercube sampling, Lion Pride Optimization, and finite element analysis to predict and optimize the flexural 13 14 properties of APCC. The framework was implemented into designing APCC beams, which were fabricated via 3D printing and tested under flexural loads. Results show that the designed APCC 15 achieved high specific flexural strength and high specific toughness. The architecture of APCC 16 17 arrests crack propagation and promotes energy dissipation. Parametric studies were performed to evaluate the effect of the key design variables of APCC beams on the flexural properties. This 18
- 20 Keywords: AI-assisted design of materials; architectured polymer-concrete composite (APCC);

research advances the knowledge and development of APCC.

- 21 high strength and high toughness material; Latin hypercube sampling; Lion Pride Optimization;
- 22 sequential surrogate modeling

19

#### 1. Introduction

23

24

25

26

27

28

29

30

31

32

33

34

35

36

37

38

39

40

41

42

43

44

45

Concrete is the most widely used structural material worldwide. The annual consumption of concrete is 30 billion tons [1]. Compared with other structural materials such as steel and wood, concrete has important advantages ranging from constructability to mechanical properties and durability. Fresh concrete is flowable and can cast desired geometries and volumes of structures, which is challenging when steel or wood is used. For example, concrete can be used to fabricate curved façade [2] and large dams [3]. Concrete also owns high compressive strength, high fire resistance, high availability, low cost, low thermal conductivity, and long durability. However, concrete is brittle and weak in tension, making concrete easy to crack and fail in tension/flexure. The current methods used to enhance the tensile and flexural properties of concrete can be categorized into two types: (1) Continuous reinforcement such as bars, tendons, and meshes, which can be made using materials with high tensile properties such as steel and fiber-reinforced polymer (FRP). The most popular types of FRP utilized to reinforce concrete are carbon FRP (CFRP) and glass FRP (GFRP) [4]. Compared with steel, FRP has lower density, higher tensile strength, and higher corrosion resistance, but FRP is often brittle and ruptures suddenly, without exhibiting a large elongation before failure. (2) Discrete reinforcement such as chopped fibers and nanofibers/nanotubes. Popular chopped fibers used in concrete include steel fibers [5, 6] and synthetic polymer fibers [7], which are mixed into concrete to make fiber-reinforced concrete. The chopped fibers enhance the crack resistance through a bridging effect [8]. Representative examples of high-performance fiber-reinforced cementitious composites (HPFRCC) include ultra-high-performance concrete (UHPC) and engineered cementitious composites (ECC) [9-11]. Recently, nanomaterials have been incorporated into concrete to supplement chopped fibers and provide multi-scale reinforcement for multi-scale cracks [12].

The above two categories of reinforcing solutions have been widely applied since they are aligned with the current structural design and construction methods. In the design of beams with continuous reinforcement, longitudinal bars usually near the top and/or bottom surfaces subject to the largest stresses. Such a philosophy simplifies design and facilitates the construction. When discrete reinforcement is used, it can be directly added during concrete mixing, without having to significantly modify the construction process. However, adding fibers to concrete often reduces the flowability [13], so effective measures should be taken to improve the workability [14]. It is essential to control the dispersion and orientation of reinforcing fibers. Uneven fiber dispersion generates weak spots that reduce the crack resistance of concrete [15-17]. The fiber orientation directly affects the tensile properties of concrete [18].

Recent advances in manufacturing and construction have created opportunities to develop novel solutions of reinforcing concrete for high mechanical performance. The unique capability of three-dimensional (3D) printing for manufacturing spatially-complex geometries has enlarged the design space of continuous reinforcement. The spatial layout of continuous reinforcement has gone beyond 1D straight bars and 2D plane meshes because 3D lattices have been printed to fabricate architectured composites [19-23]. Salazar et al. [24] proposed 3D polymeric lattices fabricated using polylactic acid (PLA) or acrylonitrile butadiene styrene (ABS) and used to fabricate polymer-concrete composite (PCC) which achieved strain-hardening properties and multiple cracks. Xu and Šavija [25] fabricated ABS reinforcement meshes via 3D printing and found that the use of fine meshes in concrete achieved strain-hardening properties, while the use of coarse meshes led to a single crack in concrete beams. A few studies have been conducted to explored the auxetic properties of composites with metal lattices filled with mortar or concrete [26-29], and found that the impact resistance was increased by auxetic architectures [26, 29].

Previous studies demonstrated that it is feasible to use 3D printed polymer reinforcement to enhance the flexural performance of concrete. When the polymer parts are properly designed, the PCC can achieve strain-hardening properties and multiple cracks [25]. The light weight and high corrosion resistance of polymer make it promising to develop lightweight and durable structures. Another lesson learned from prior studies is that the mechanical properties of PCC are related to the geometry and dimensions of polymer lattices [25]. To date, the effects of the design variables of polymer lattices on the mechanical properties of PCC and the mechanisms are still unclear.

To address the knowledge gap, this research aims to: (1) develop an optimization framework to promote the design of PCC by integrating finite element analysis, Latin hypercube sampling (LHS), sequential surrogate modeling, and Lion Pride Optimization (LPO); (2) implement the framework into the design of architectured PCC (APCC) with high specific flexural strength and high specific toughness; and (3) understand the fracture mechanism of APCC and investigate the effects of design variables on the flexural strength and toughness of APCC.

The remainder of the paper is organized as follows: Section 2 presents the methods and the optimization framework; Section 3 elaborates the experimental and simulation results and the underlying fracture mechanism of APCC for enhancing the specific flexural strength and specific toughness; Section 4 presents the optimal design of APCC; and Section 5 concludes the findings.

#### 2. Methods

The methods adopted in this paper are elaborated in four subsections: Section 2.1 overviews the optimization framework; Section 2.2 presents the design of APCC with high specific flexural properties; Section 2.3 elaborates on the manufacturing and experimental testing of APCC beams; and Section 2.4 elaborates on the finite element model and the investigated cases used to evaluate the effect of design variables on the flexural properties of APCC.

#### 2.1. Overview

An optimization framework is presented to designing APCC with high specific flexural strength and high specific toughness. The flowchart of the framework is shown in **Fig. 1**. The optimization framework includes three steps: (1) A dataset is generated to relate the mechanical properties of APCC to the key design variables via finite element analysis [30] based on LHS [31] (Section 2.2.2). (2) The dataset is utilized to develop a sequential surrogate model [32] for predicting the flexural properties of APCC (Section 2.2.3). (3) The predictive model is integrated with LPO [33] for determining the optimal design of APCC (Section 2.2.4). Based on this framework, this research developed finite element models to investigate the effect of design variables on the mechanical properties of APCC and the underlying mechanisms (Section 2.4). The proposed method was validated using experimental testing data (Section 2.3).

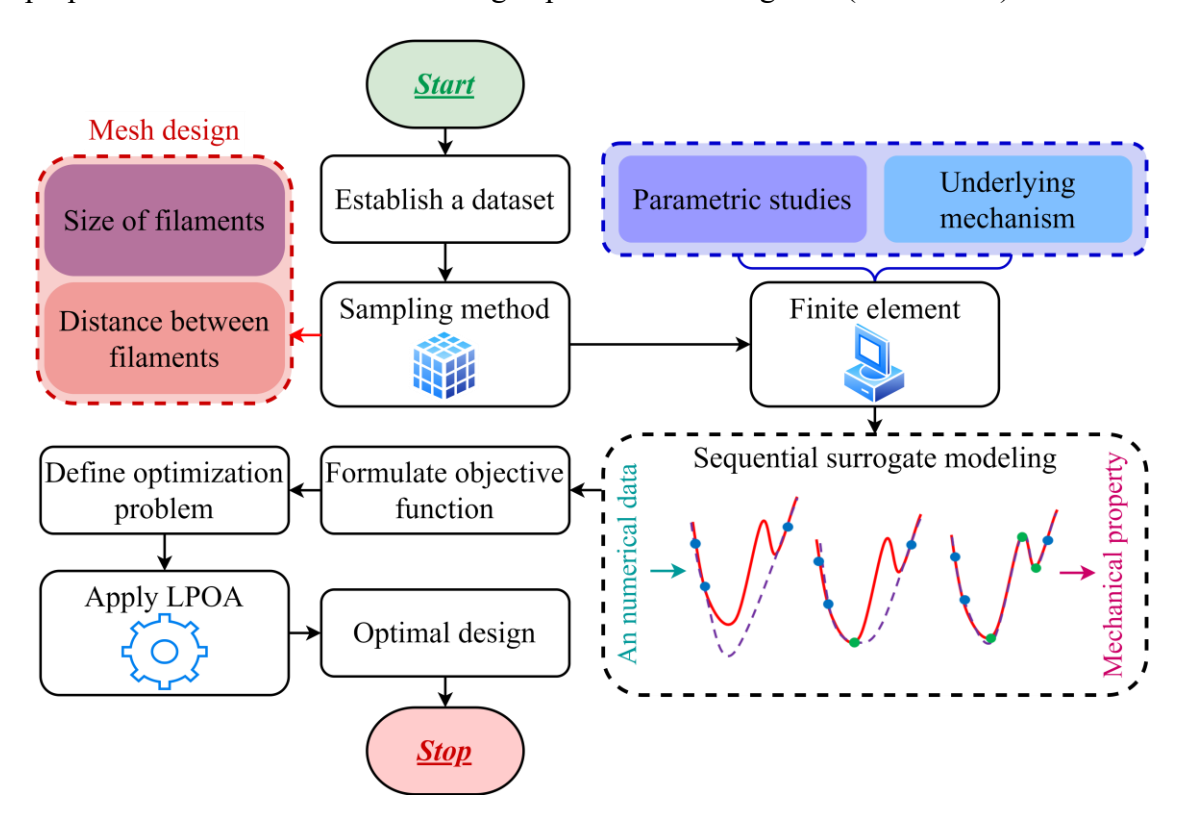


**Fig. 1.** Flowchart of the proposed machine learning-aided optimization framework for designing APCC with high specific flexural strength and high specific toughness.

# 2.2. Design method

# 2.2.1. Initial design

The envisioned APCC is composed of architectured polymer lattices and concrete matrix, as shown in Fig. 2. The APCC is fabricated in two steps. First, a lattice structure is fabricated using a 3D printer and polymer filaments. Then, the polymer lattice is placed in a mold, and concrete is poured to cast APCC. A detailed description of the fabrication process is provided in Section 2.3.

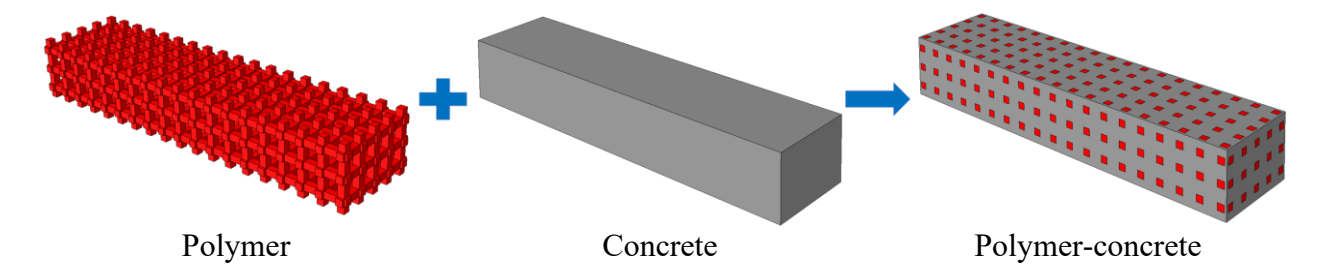


Fig. 2. Main structure of the APCC composed of architectured polymer lattices and concrete.

In the initial design, the main consideration is the manufacturability: (1) It is feasible and efficient to manufacture architectured polymer lattices through 3D printing [34]. It is desired to use consistent filaments with minimal overhanging parts. (2) It is convenient to cast concrete to fill the voids of architectured polymer lattices. The voids of the architectured polymer lattices should be interconnected and large enough for fresh concrete to fill and consolidate.

An initial design and the design variables are shown in **Fig. 3**. The design variables include: (1) the spacings between adjacent filaments, designed by  $d_x$ ,  $d_y$ , and  $d_z$ , which are the spacing between adjacent filaments along X, Y, and Z; and (2) the sizes of filaments, designed by  $v_x$ ,  $v_y$ , and  $v_z$ , which are the width of each filament along X, Y, and Z. In the initial design, the spacing between adjacent filaments ( $d_x$ ,  $d_y$ , and  $d_z$ ) is 15 mm along X, Y, and Z; and the width of each filament ( $v_x$ ,  $v_y$ , and  $v_z$ ) is 5 mm along X, Y, and Z. The concerned properties are the specific flexural strength ( $\delta$ ) and specific toughness ( $\beta$ ), as defined in Eq. (1) and Eq. (2):

$$\delta = \frac{S}{D} \tag{1}$$

$$\beta = \frac{T}{D} \tag{2}$$

where  $\delta$  and  $\beta$  are the specific flexural strength and specific toughness of APCC, respectively; S is the flexural strength of APCC; T is the toughness of APCC, defined as the area under the load-displacement curve; and D is the density of APCC.

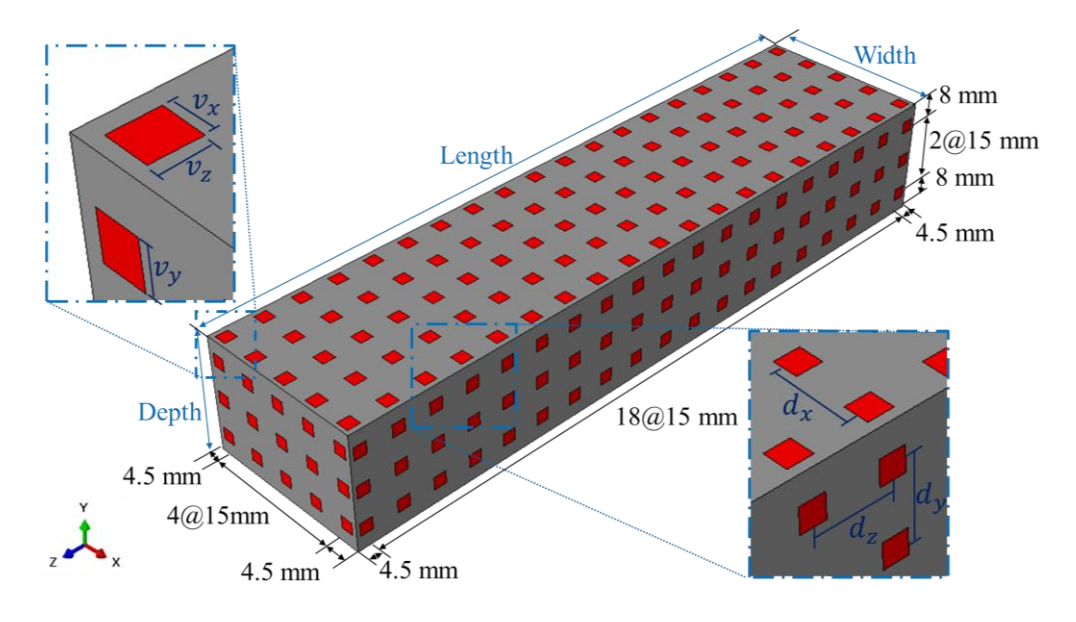


Fig. 3. Initial design and definition of the design variables of APCC scalable for large structures.

To assess the performance of the initial design of APCC, five APCC beam specimens were fabricated and tested under four-point bending until failure, as elaborated in Section 2.3. The experimental results were then compared with the finite element analysis results obtained, as elaborated in Section 3.

## 2.2.2. Establishment of dataset

To optimize the design of APCC, it is necessary to establish a dataset of various designs of APCC and the corresponding flexural properties. In this research, finite element analysis was conducted using a commercial software, namely ABAQUS [30], to establish the dataset. The finite element model and model validation are elaborated in Sections 2.4 and Section 3,

respectively. The design variables of APCC were used as the input variables. The flexural properties of APCC were the output variables. The input variables were sampled using the LHS method [31], which is a statistical method that selects samples randomly in the sampling space. The LHS method was effective in reducing the number of sampling points [35]. The recommended number of initial samples was 10 times the number of design variables [36]. In this research, six design variables were considered, so the number of initial finite element models was 60. With the sampled input variables of APCC, the flexural properties of APCC were determined through finite element analysis. After the dataset was generated, it was split into a training set and a validation set.

## 2.2.3. Sequential surrogate model

This study developed a sequential surrogate model to approximate the behavior of complex systems [32]. As a machine learning technique, a sequential surrogate model is utilized when the system is computationally expensive such as 3D nonlinear finite element analysis that considers nonlinear material properties and damages, which make the finite element models difficult to converge. Thus, this research used a sequential surrogate model to predict the flexural properties of APCC. In the operation of the sequential surrogate model, new sampling points are iteratively added to the training set based on a sequential sampling technique. This process is recognized as an active learning/training process, which allows the sequential surrogate model to improve when more data becomes available [37]. The concept of sequential surrogate models is shown in Fig. 4. The methods of Expected Improvement (EI) [38, 39] and Mean Square Error (MSE) [40] were utilized to establish the standards for selecting more samples that are used to enlarge the training set and enhance the efficiency of sequential surrogate models. More details about infill criteria for expanding the training set are elaborated in Section 2.2.3.2.

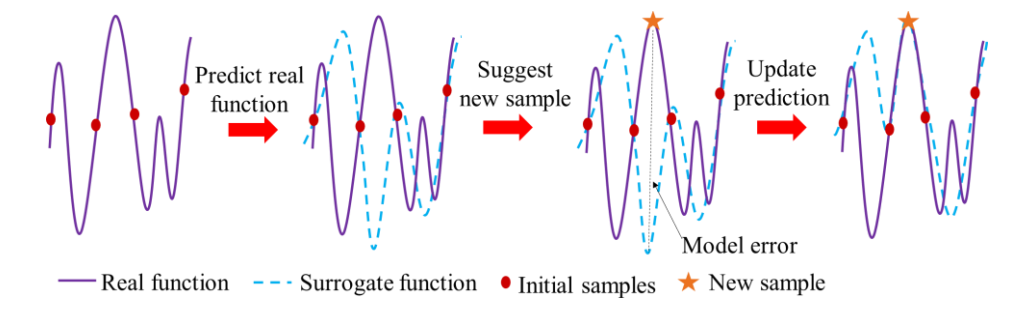


Fig. 4. Concept of the sequential surrogate modeling technique employed to design APCC.

The flowchart for establishing the sequential surrogate model is shown in **Fig. 5**. There are five main steps [41]: (1) Establish the training and validation datasets (Section 2.2.2). (2) Train the surrogate model using the training dataset (Section 2.2.3). (3) Test the performance of the trained predictive model using the validation dataset that is unseen in the training process. Two performance metrics, the Coefficient of Determination ( $R^2$ ) and the Root Mean Square Error (*RMSE*), are employed to quantify the accuracy of the surrogate model (Section 2.2.3.1). (4) Improve the performance of the trained surrogate model by adding more samples to the training dataset using two infill criteria, namely *EI* and *MSE* (Section 2.2.3.2). (5) Repeat Steps 3 to 5 until the stopping criteria are met. Two stopping criteria are defined in Section 2.2.3.2.

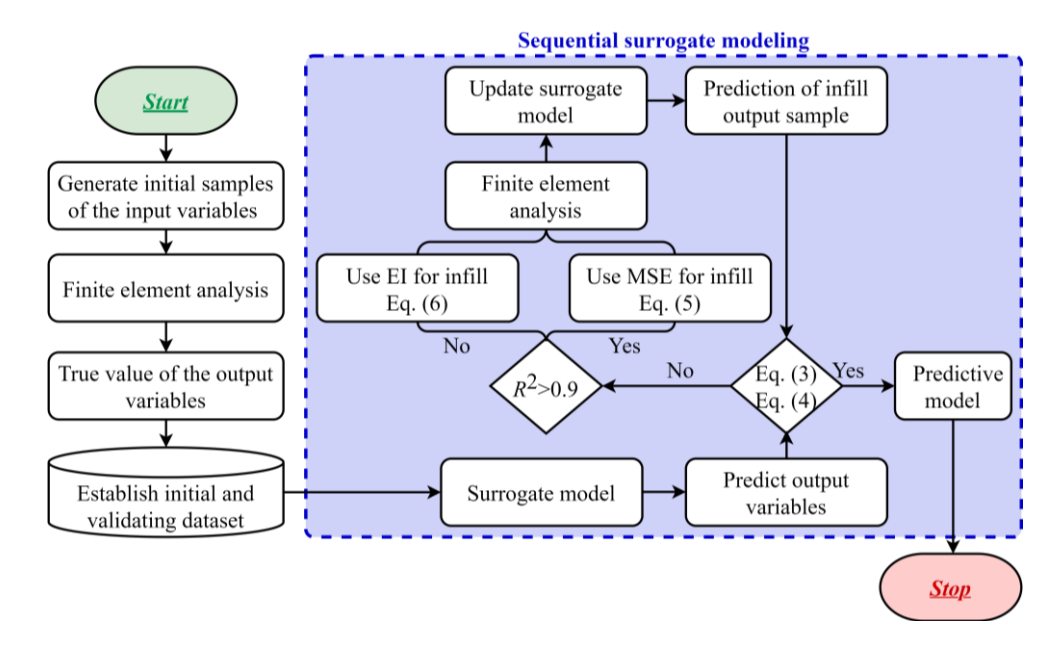


Fig. 5. Process of the sequential surrogate modelling for predicting and optimizing APCC.

#### 2.2.3.1. Performance metrics

175

180

183

189

in Eq. (8).

Two performance metrics were utilized, which are the Coefficient of Determination ( $R^2$ ) and *RMSE*, which are defined in Eq. (3) and Eq. (4), respectively.

$$R^{2}(X,Y) = 1 - \frac{\sum_{i=1}^{n} (x_{i} - y_{i})^{2}}{\sum_{i=1}^{n} [y_{i} - mean(y_{i})]^{2}}$$
(3)

$$RMSE(X,Y) = \sqrt{\frac{\sum_{i=1}^{n} (x_i - y_i)^2}{n}}$$
 (4)

where  $X = \{x_1, x_2, ..., x_n\}$  denote the predicted values;  $Y = \{y_1, y_2, ..., y_n\}$  denote the actual values; and n denotes the number of observed data points.

## 2.2.3.2. Stopping and infill criteria

The stopping criterion determines when the training process is terminated. Two specific stopping criteria shown in Eq. (5) and Eq. (6) are utilized:

$$R_i^2 \ge R_{Thresh}^2 \tag{5}$$

$$|RMSE_i - RMSE_{i+1}| \le \Delta RMSE_{Thresh}(1 + |RMSE_i|) \tag{6}$$

stopping criteria.  $R_{Thresh}^2$  and  $\Delta RMSE_{Thresh}$  are 0.91 and 0.06×10<sup>6</sup> kN·mm<sup>3</sup>/kg, respectively.

To improve the accuracy of the surrogate predictive model, in the training process, more samples were added to the training dataset before the stopping criteria were met. Two infill criteria were applied: When  $R^2$  is below 0.9, new samples are added using MSE, as defined in Eq. (7). When  $R^2$  is greater than or equal to 0.9, new samples are added using EI, as defined

where subscript i is the quantity of infill samples, and subscript Thresh is the threshold of the

$$\hat{S}^{2}(y(x^{*})) = \sigma^{2}(1 - t^{\varphi}\varphi^{-1}t) \tag{7}$$

$$EI(x) = \frac{y_{min} - \hat{y}(x^*)}{2} \left[1 + erf\left(\frac{y_{min} - \hat{y}(x^*)}{\sqrt{2}\hat{S}^2[y(x^*)]}\right)\right] + \frac{\hat{S}^2[y(x^*)]}{\sqrt{2\pi}} \exp\left[\frac{\hat{y}(x^*) - y_{min}}{2\hat{S}^2[y(x^*)]}\right]$$
(8)

where  $\sigma^2$  is the dispersion in the mean of the predictive model;  $\varphi$  is the correlation matrix between two given input variables; t is the correlation between a newly added sample and the existing samples in the training dataset;  $y_{min}$  is the current optimal value; erf is to the error function;  $y(x^*)$  is the predicted value of the new sample;  $\hat{y}(x^*)$  and  $\hat{S}^2[y(x^*)]$  are the mean and variance of the random Gaussian process, respectively.

## 2.2.4. Optimization method

The design of APCC was formulated as an optimization problem that aims to maximize the specific flexural strength and the specific toughness. **Table 1** lists six design variables and their ranges, which were determined based on the highest values of the specific flexural strength and the specific toughness in a parametric study while considering manufacturability (Section 3.1).

**Table 1.** Ranges of the design variables

	Tuble 1. Italiges of the design vari	
Number	Design variables	Range (mm)
1	$v_x$	1-12
2	$v_{\mathcal{y}}$	1-12
3	$v_z$	1-12
4	$d_x$	10-40
5	$d_{\mathcal{Y}}$	10-40
6	$d_z$	10-40

In the optimization process, to ensure an appropriate consolidation of concrete, a design constraint was imposed to enforce that the spacings between adjacent polymer filaments are not less than 10 mm, which is considered sufficiently large to fill with the mortar. A penalty function approach was adopted to transform the constrained optimization problem into an unconstrained optimization problem. A penalized objective function  $F_{Penalty}$  is defined as the product of the original objective function F and a penalty function  $F_{penalty}$ .

$$F_{Penalty} = F \times f_{penalty} \tag{9}$$

$$f_{nenalty} = \left[1 + \gamma_1 \times (\omega_x + \omega_y + \omega_z)\right]^{\gamma_2} \tag{10}$$

$$\omega_{i} = \begin{cases} \sum_{i=1}^{n} \left(1 - \frac{d_{i_{max}}}{d_{i}}\right) & \text{if } \omega_{i} > d_{i_{max}} \\ 0 & \text{if } \omega_{i} \leq d_{i_{max}} \end{cases}$$
(11)

where  $d_i$  is the spacing between adjacent filaments;  $d_{imax}$  is the upper boundary value constraint for the variable  $d_i$ ;  $\gamma_1$  and  $\gamma_2$  are two constants; and  $\omega_i = \{\omega_x, \omega_y, \omega_z\}$  is the extent of violation of design limits. In this study,  $\gamma_1$  was fixed at 1.0, and  $\gamma_2$  gradually increased from 1.3 to 3.0 in the optimization process, following the approach described in reference [42].

The optimization task was solved using the LPO algorithm [33], which is a nature-inspired metaheuristic algorithm. The numbers of generations and population size of the LPO were set to 300 and 100, respectively.

#### 2.3. Experiments

Seven APCC beams, including five beams with the initial design of APCC and two beams with the optimal design of APCC, were fabricated for flexural tests. The optimal design was determined using the proposed method as described in Section 2.2. More details about the design optimization are available in Section 4.

The beam specimens were fabricated in two steps. First, architectured ABS lattices were printed through Fused Deposition Modeling (FDM) [43] using a commercial 3D printer (model: Flashforge Guider II). Computer models of ABS lattices were created and saved as stereolithography (STL) files, which were utilized to produce ABS lattices layer by layer, as illustrated in **Fig. 6**. The ABS filament was heated to a semi-molten state and then pushed through the nozzle to create 2D slices layer by layer. The parameters used in the 3D printing process are listed in **Table 2**. The density and Poisson's ratio of ABS are 792 kg/m<sup>3</sup> and 0.35, respectively. This study adopted ABS as the polymer material to develop the methods. Other polymers can be used to replace ABS in future investigations.

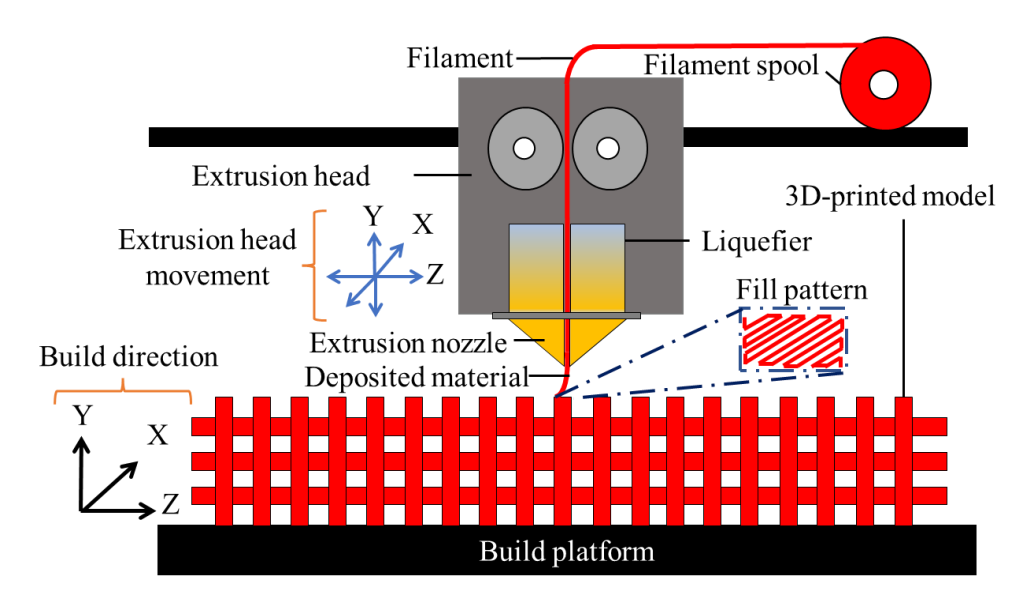


**Fig. 6.** Fabrication of 3D polymer lattices for APCC based on the 3D printing through FDM.

Table 2. Parameters of 3D printing

Table 2. I arame	ters of 3D printing
Printing parameter	Configuration
Nozzle diameter	0.4 mm
Layer thickness	0.1 mm
Maximum speed	70 mm/s
Minimum speed	5 mm/s
Temperature	240 °C
Infill density	100%
Fill pattern	Line
Filament material	ABS

The polymer lattices were placed in beam molds, followed by casting concrete. Each mold measured 76 mm × 50 mm × 300 mm and was oiled before the placement of polymer lattices. The concrete represents a typical construction mortar. The formulation is listed in **Table 3**. The water-to-binder ratio was 0.45. The binder was composed of Type I Portland cement and slag sourced from a local supplier in New Jersey, USA. The chemical compositions and physical characteristics of the Portland cement, slag, and river sand are listed in **Table 4**. To improve the flowability, a high-range water reducer was used. The mini-slump spread was 300 mm, which is sufficient to achieve self-consolidation without having to apply external vibration. The compressive strength was evaluated using cubic

specimens (50 mm  $\times$  50 mm) according to ASTM 109 C [44]. Each test was replicated three times. The compressive strength at 7 days was 35 MPa  $\pm$  3 MPa. The density and Poisson's ratio were 2500 kg/m<sup>3</sup> and 0.2, respectively. The elastic modulus was evaluated in accordance with ACI 318 [45].

Table 3. Mixture design of concrete

Type I Portland cement	Slag	River sand	Water	HRWR
739.4	0	1244.1	295.7	3.0

**Table 4**. Chemical and physical properties of the dry ingredients of concrete

	1 1 1		
Components	Type I Portland cement	Slag	River sand
$\mathrm{SiO}_{2}\left(\% ight)$	22.44	36.21	80.30
$Al_2O_3$ (%)	2.76	11.10	10.50
Fe <sub>2</sub> O <sub>3</sub> (%)	2.24	0.76	3.43
CaO (%)	68.05	43.75	1.72
MgO (%)	0.91	5.09	1.70
$SO_3$ (%)	2.25	2.21	1.07
$Na_2O(\%)$	0.19	0.23	-
$K_2O(\%)$	0.11	0.40	-
$TiO_2$ (%)	0.14	0.58	-
$P_2O_5$ (%)	0.09	0.02	-
$Mn_2O_3$ (%)	0.03	0.36	-
C <sub>3</sub> S (%)	62.35	-	-
C <sub>2</sub> S (%)	20.28	-	-
C <sub>3</sub> A (%)	1.42	-	-
$C_4AF$ (%)	5.83	-	-
Loss of ignition (%)	1.28	0.72	1.28
Specific gravity (g/cm <sup>3</sup> )	3.15	2.9	2.65

Immediately after concrete casting, the beams were covered by plastic sheets to avoid moisture loss. The beams were kept in molds for 24 hours. After the molds were removed, the beams were stored in a curing tank with a lime-saturated solution. After the beams were cured for 7 days, they were air dried for 24 hours (room temperature:  $20 \pm 2$  °C; relative humidity:  $50\% \pm 5\%$ ).

The beams were then tested until failure with a four-point bending test setup, as shown in **Fig. 7**. The beams were supported by two rollers and loaded by two other rollers that were attached to a universal load frame (model: Instron 5960). The span length was 260 mm, and

the load spacing was 94 mm. The tests were conducted under a displacement control mode with a displacement rate of 1 mm/min. The deflections of the beam was monitored using displacement sensors. The loading was terminated after the carried load dropped to below 85% of the peak load.

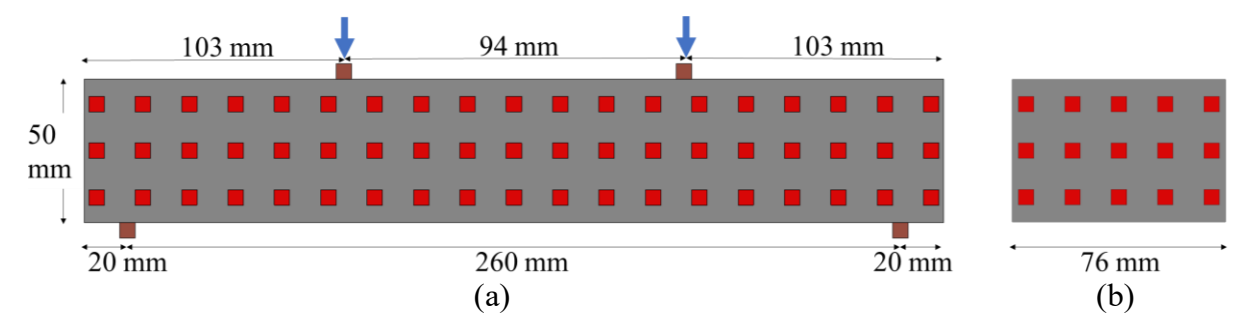
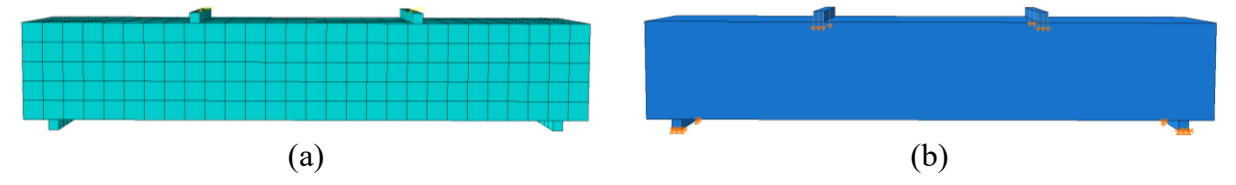


Fig. 7. Example of APCC beams under four-point bending: (a) front view, and (b) side view.

## 2.4. Finite element analysis

The mechanical behavior of APCC beams was analyzed via 3D finite element analysis, as shown in Fig. 8 [30]. A mesh sensitivity analysis was conducted to determine a proper mesh size, which was 5 mm. Concrete and polymer lattices were modeled using 3D eightnode solid elements with reduced integration (C3D8R). The interaction between polymer and concrete was defined with a keyword "embed", without considering interfacial debonding. The boundary conditions of beams were consistent with the tests. Vertical loads were applied under displacement control. The energy dissipation of concrete and polymer was considered by defining Energy Dissipated per unit Volume by Plastic Deformation (EPDDEN) in the history output.



**Fig. 8.** Finite element model of the beams: (a) meshed model, and (b) loading and boundary conditions.

The constitutive relationships of concrete and ABS are shown in **Fig. 9**. The damages of concrete were considered using a Concrete Damaged Plasticity (CDP) model, which has been utilized to consider compressive and tensile damages of concrete, as shown in **Fig. 9(a)**. The parameters of the CDP model are listed in **Table 5**. More details of the CDP models are available in references [46, 47].

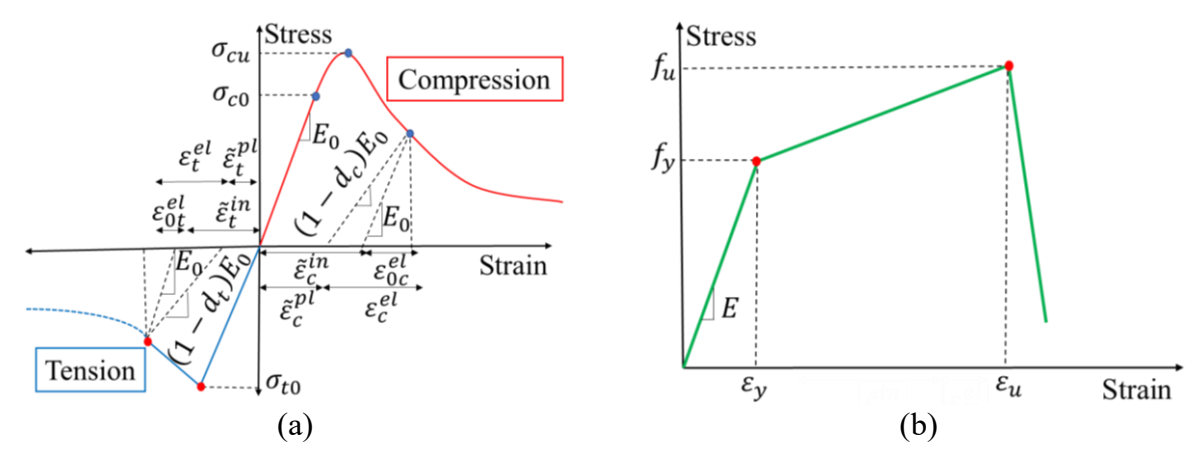


Fig. 9. Constitutive relationships of the used materials: (a) concrete [48]; and (b) ABS [49].

**Table 5.** Parameters of the adopted CDP model

Density (kg/m³)	Poisson's ratio	Young's modulus (GPa)	Dilation angle	Eccentricity	fb <sub>0</sub> /fc <sub>0</sub>	K	Viscosity parameter
2500	0.2	30	31	0.1	1.16	0.67	0

The ABS was considered as a ductile material, and the tensile properties were modelled using a multi-linear model, as shown in **Fig. 9(b)**. The mechanical properties of ABS are listed in **Table 6**. The density of ABS was 792 kg/m<sup>3</sup>.

**Table 6.** Mechanical properties of ABS

Young's modulus	Doiggon's	Viold strongth	Ultimate	Plastic	Γ	Ouctile dama	ge
(GPa)		(MPa)	strength (MPa)	strain	Fracture	Stress	Strain
(Gra)	ratio	(MFa)	sueligiii (MFa)	Strain	strain	triaxiality	rate
2.4	0.35	25.77	33.32	0.0455	0.05	0.333	0.0002

## 2.4.1. Parametric study

Based on the finite element model, the effect of the variables of the polymer lattices on the flexural properties of APCC was evaluated via a parametric study, as listed in **Table 7**.

286

287

288

289

290

291

292

293

**Table 7.** Investigated cases in the parametric study

Design	Designation	$v_{x}$	$v_{y}$	$v_z$	$d_x$	$d_y$	$d_z$
variables	Initial	5	5	5	15	15	15
	$v_x$ -1	1	5	5	15	15	15
17	$v_x$ -3	3	5	5	15	15	15
$v_{x}$	$v_x$ -7	7	5	5	15	15	15
	$v_x$ -9	9	5	5	15	15	15
	$v_y$ -1	5	1	5	15	15	15
11	$v_y$ -3	5	3	5	15	15	15
$v_{y}$	$v_y$ -7	5	7	5	15	15	15
	$v_y$ -9	5	9	5	15	15	15
	$v_z$ -1	5	5	1	15	15	15
44	$v_z$ -3	5	5	3	15	15	15
$v_z$	$v_z$ -7	5	5	7	15	15	15
	$v_z$ -9	5	5	9	15	15	15
	$d_x$ -10	5	5	5	10	15	15
$d_x$	$d_x$ -20	5	5	5	20	15	15
$u_{\chi}$	$d_x$ -25	5	5	5	25	15	15
	$d_x$ -30	5	5	5	30	15	15
	$d_y$ -10	5	5	5	15	10	15
d	$d_{y}$ -20	5	5	5	15	20	15
$d_{\mathcal{y}}$	$d_y$ -25	5	5	5	15	25	15
	$d_{y}$ -30	5	5	5	15	30	15
	$d_z$ -10	5	5	5	15	15	10
d	$d_z$ -20	5	5	5	15	15	20
$d_z$	$d_z$ -25	5	5	5	15	15	25
	$d_z$ -30	5	5	5	15	15	30

The number of polymer filaments along X, Y, Z direction can be computed as:

$$N = Round \ down\left(\frac{K - V}{D}\right) + 1 \tag{14}$$

where  $N = \{n_x, n_y, n_z\}$  is the number of polymer filaments;  $K = \{k_x, k_y, k_z\}$  is the dimension of an APCC beam;  $V = \{v_x, v_y, v_z\}$  is the polymer filament dimensions; and  $D = \{d_x, d_y, d_z\}$  is the spacing between adjacent polymer filaments.

# 3. Experimental and Simulation Results

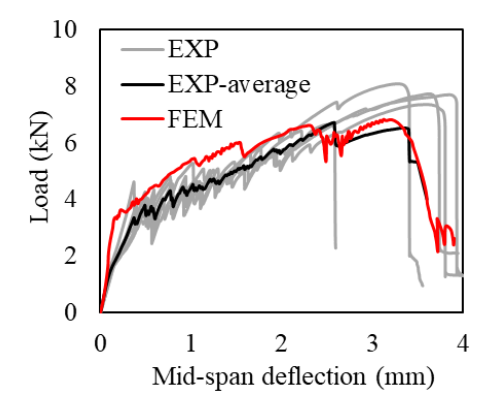
The failure patterns of the five beams fabricated according to the initial design of APCC are shown in **Fig. 10**. Vertical flexural cracks were observed from the flexural span of each

beam. The cracks initiated from the bottom and then extend to the top of the beams with the increase of the load levels. Some horizontal cracks were observed from the middle depth of the beams. The positions of cracks were well correlated with the positions of the polymer lattices. The widths of the cracks were in the range of 20  $\mu$ m to 50  $\mu$ m when they were initiated and then increased with the increase of the applied load. After the beams failed, the fracture sections were inspected. It was found that polymer lattices were embedded in concrete and ruptured at the fracture sections.



Fig. 10. Distribution of cracks and crack section of APCC beams based on the initial design.

The load versus mid-span deflection curves of the five beams are plotted in Fig. 11. The load first linearly increased with deflection at the beginning. After the concrete was cracked, the load continued increasing, but the load increasing rate was reduced. The load-deflection curves show that the beams achieved strain-hardening properties which can be attributed to the use of ABS lattices because concrete is brittle. With the increase of deflection, more and more cracks were generated in concrete. The generation of more cracks are reflected by the fluctuations of loads in the load-deflection curves. Finally, the beams fractured, and the load decreased to zero. The finite element analysis results are compared with the test results, and their good agreement indicates that the finite element model provided reasonable predictions of the flexural behavior of the APCC beam.



312

313

314

315

316

Fig. 11. Experimental (EXP) and finite element analysis (FEM) results of the APCC beams.

# 3.1. Parametric study results

The effect of the design variables  $v_x$ ,  $v_y$ ,  $v_z$ ,  $d_x$ ,  $d_y$ , and  $d_z$  on the flexural behavior of

APCC beams is shown in Fig. 12. All APCC beams show strain-hardening behaviors.

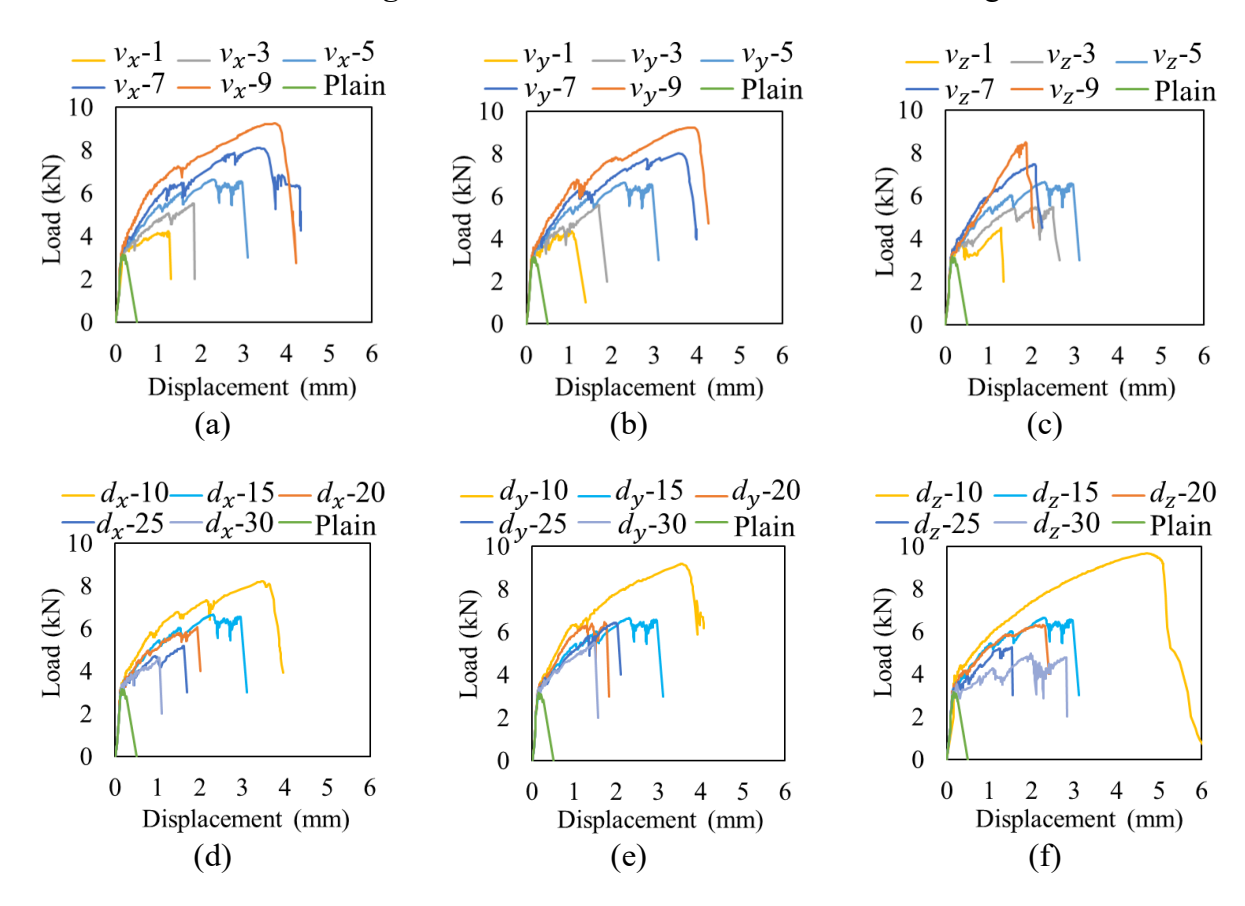


Fig. 12. Load-deflection curves of APCC beams with different (a)  $v_x$ , (b)  $v_y$ , (c)  $v_z$ , (d)  $d_x$ ,

318 (e)  $d_y$ , and (f)  $d_z$ .

317

The specific flexural strength ( $\delta$ ) and specific toughness ( $\beta$ ) of the investigated APCC beams are summarized in **Table 8**. Increasing the dimensions of ABS filaments along X and Y directions ( $v_x$  and  $v_y$ ) increases  $\delta$  and  $\beta$ . Specimens  $v_x$ -9 and  $v_y$ -9 exhibit the highest  $\delta$  and  $\beta$ . Increasing the dimensions of ABS filaments along Z direction ( $v_z$ ) increases  $\delta$ . Specimen  $v_z$ -9 exhibits the highest  $\delta$ . When  $v_z$  is less than 5 mm,  $\beta$  increases with  $v_z$ . However, when  $v_z$  is larger than 5 mm,  $\delta$  decreases with  $\delta$  specimen  $\delta$  has the highest  $\delta$  overall, increasing the spacings between ABS filaments decreases  $\delta$  and  $\delta$ . Specimens  $\delta$  specimens  $\delta$  and  $\delta$  specimens  $\delta$  specimens  $\delta$  and  $\delta$  specimens  $\delta$  specimens  $\delta$  and  $\delta$  specimens  $\delta$  specimens

**Table 8.** Mechanical properties of the investigated APCC beams

- D :	1 abic 0				vestigated APCC t	
Design	Designation	Density	Strength	Toughness	δ	β
variables		$\frac{(kg/m^3)}{2210}$	(kN)	(kN·mm)		$(\times 10^6 \text{ kN} \cdot \text{mm}^4/\text{kg})$
	$v_x$ -1	2310	4.21	4.41	1.79	1.88
	$v_x$ -3	2226	5.53	7.81	2.35	3.32
$v_x$	$v_x$ -5	2142	6.64	16.4	3.03	7.66
	$v_x$ -7	2058	8.10	27.55	3.45	11.72
	$v_x$ -9	1973	9.25	34.50	3.93	14.70
	$v_y$ -1	2299	4.36	4.08	1.86	1.74
	$v_y$ -3	2220	5.59	7.25	2.39	3.10
$v_y$	$v_y$ -5	2142	6.64	16.4	3.03	7.66
	$v_y$ -7	2063	8.02	26.66	3.43	11.40
	$v_y$ -9	1985	9.23	31.80	3.95	13.60
	$v_z$ -1	2312	4.49	4.46	1.91	1.90
	$v_z$ -3	2227	5.49	11.31	2.33	4.81
$v_z$	$v_z$ -5	2142	6.64	16.4	3.03	7.66
	$v_z$ -7	2057	7.47	12.65	3.17	5.37
	$v_z$ -9	1972	8.48	11.67	3.60	4.96
	$d_{x}$ -10	2057	8.21	27.44	3.49	11.74
	$d_x$ -15	2142	6.64	16.4	3.03	7.66
$d_{x}$	$d_{x}$ -20	2184	6.05	9.23	2.58	3.93
	$d_{x}$ -25	2226	5.17	6.58	2.40	3.05
	$d_{x}$ -30	2226	4.64	3.76	2.05	1.66
	d <sub>y</sub> -10	2076	9.2	28.87	3.95	12.43
	$d_{y}$ -15	2142	6.64	16.4	3.03	7.66
$d_{y}$	$d_{y}^{2}$ -20	2207	6.46	9.18	2.76	4.10
-	$d_{y}$ -25	2207	6.44	10.20	2.52	3.40
-	$d_y$ -30	2207	5.52	6.54	2.44	3.30

	$d_z$ -10	2046	10.82	38.58	4.60	16.41
	$d_z$ -15	2142	6.64	16.4	3.03	7.66
$d_z$	$d_z$ -20	2195	6.31	12.16	2.68	5.16
	$d_z$ -25	2227	5.27	6.37	2.24	2.70
	$d_z$ -30	2248	4.97	11.06	2.11	4.70

The results of  $\delta$  and  $\beta$  are plotted in Fig. 13. Along X direction, increasing the dimension of filaments and decreasing the spacing between polymer filaments increase  $\delta$  and  $\beta$ , as shown in Fig. 13(a) and Fig. 13(d). Along Y direction, increasing  $v_y$  and decreasing  $d_y$  increase  $\delta$  and  $\beta$ , as shown in Fig. 13(b) and Fig. 13(e). Along Z direction, increasing  $v_z$  increases  $\delta$ ; and  $\beta$  first increases and then decreases with  $v_z$ , as shown in Fig. 13(c). Decreasing the spacing between polymer filaments increases  $\delta$  and  $\beta$ , as shown in Fig. 13(f). The parametric study results suggest that  $\delta$  and  $\beta$  can be increased by increasing the polymer filament dimensions (v) along X, Y and Z directions when  $v_z$  is less than 5 mm, and decreasing the spacing between adjacent ABS filaments along X, Y and Z directions.

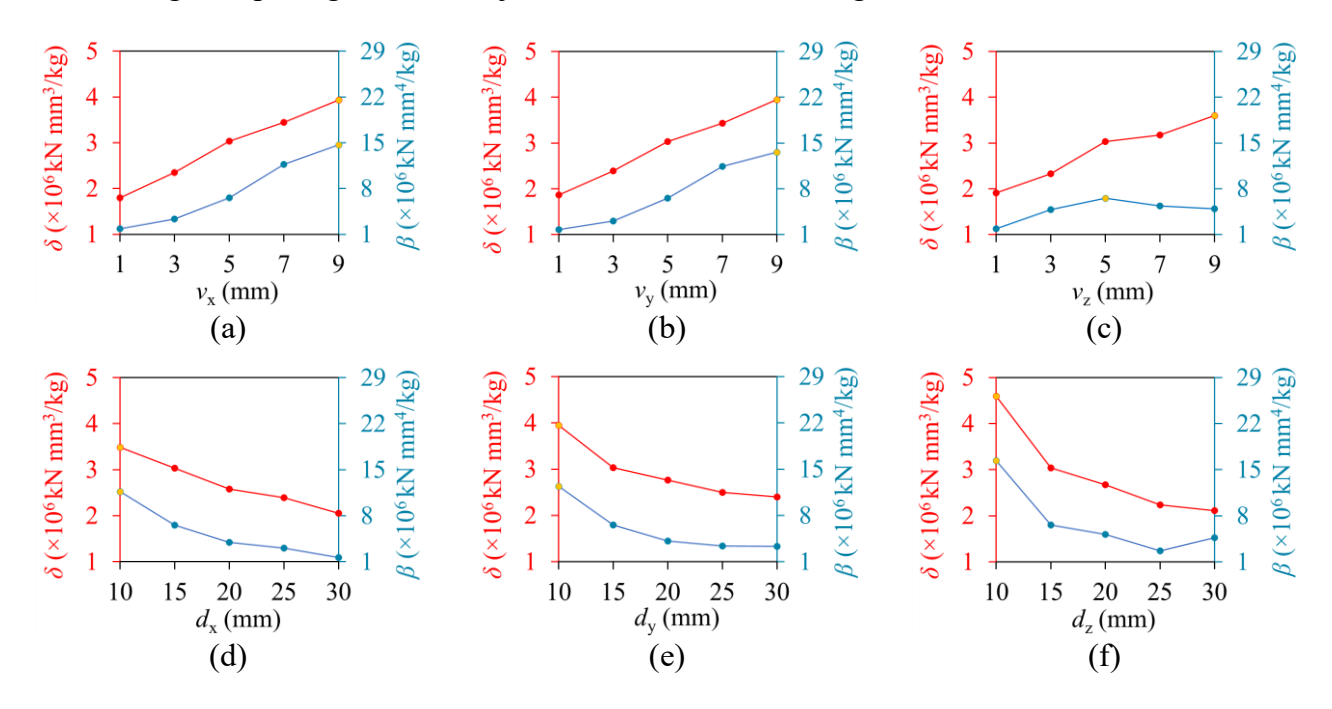
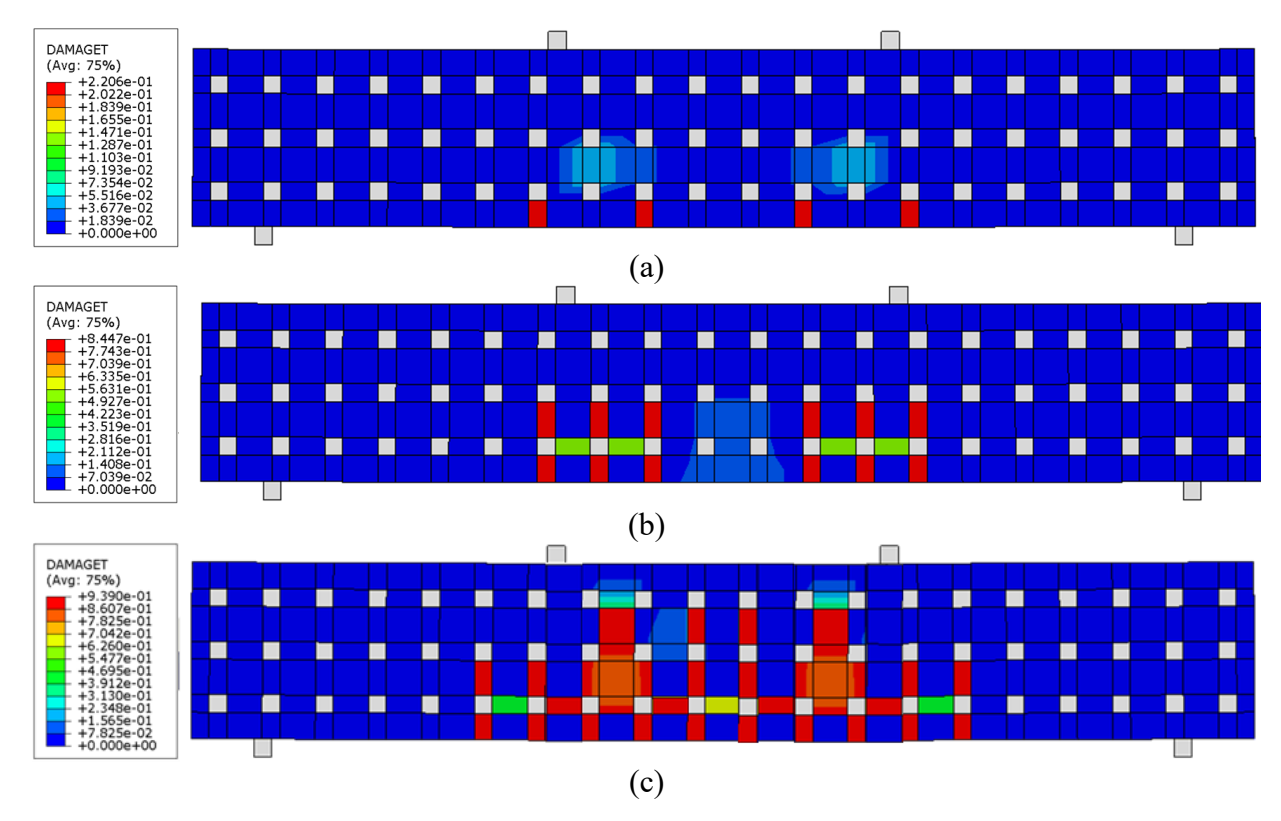


Fig. 13. Specific strength ( $\delta$ ) and specific toughness ( $\beta$ ) with varied (a)  $v_x$ , (b)  $v_y$ , (c)  $v_z$ , (d)  $d_x$ , (e)  $d_y$ , (f) and  $d_z$ .

# 3.2. Damage mechanisms

The damage process of the initial design of APCC beams is shown in **Fig. 14**. The cracks in concrete are indicated by a tension damage index (DAMAGET), which is in the range of 0 (no crack) to 1 (fully cracked). Cracks initiate from the bottom of the sections with transverse polymer filaments and propagate toward the top of the beam. The cracking process and crack patterns are consistent with the experimental testing results (Section 3). With the increase of the applied load, more cracks are generated, and the crack severity is increased. Besides the vertical cracks, horizontal cracks are also generated. Finally, the beam fails with major cracks in concrete and rupture of polymer filaments at the cracked sections.



**Fig. 14.** Development of cracks in the initial design of APCC beam under different mid-span deflections: (a) 0.6 mm, (b) 1.9 mm, and (c) 5.0 mm.

When concrete is cracked, the interaction between polymer and concrete helps arrest cracks and hinders the propagation of the cracks because of the high ductility of polymer and debonding between polymer and concrete. The debonding between ABS filaments and concrete is indicated by the horizontal cracks in the beams. The debonding helps distribute the localized deformation caused by cracks over a longer length and thus reduce the peak strain [50]. The redistribution of the crack-induced deformation thus alleviates the stress concentration at crack tips and hinders the propagation of cracks toward the top surface of the beams, as shown in **Fig. 15**. The above damage process is different from that of plain concrete, which is brittle and fractures suddenly after a crack is generated at the bottom of the beam, because the crack propagates toward the top surface of the beam rapidly due to the stress concentration at the crack tip. Such a delay of the development of cracks benefits the APCC beams by increasing their flexural strengths.

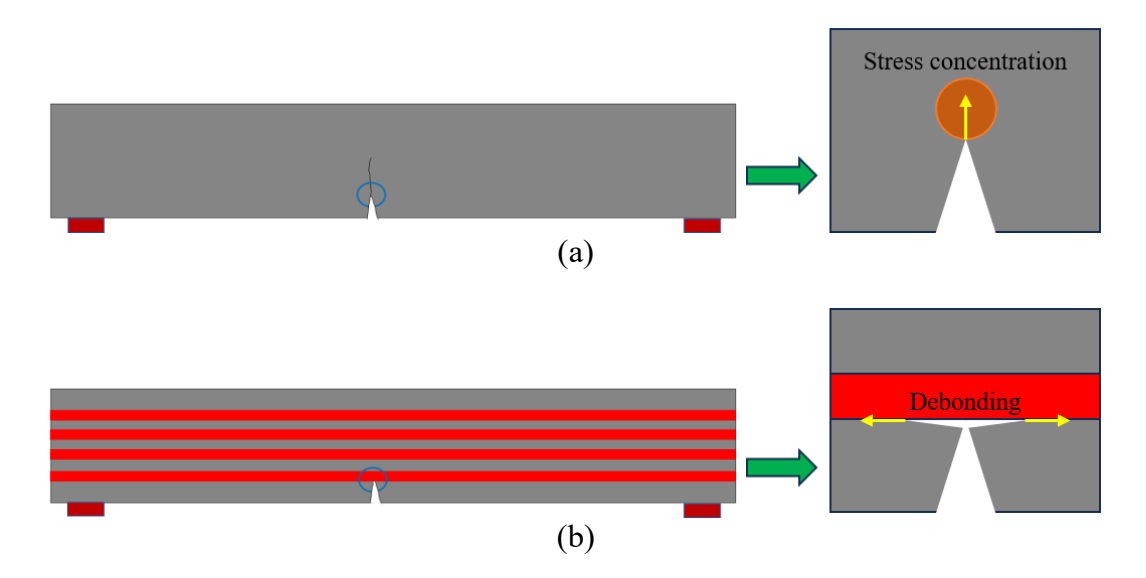
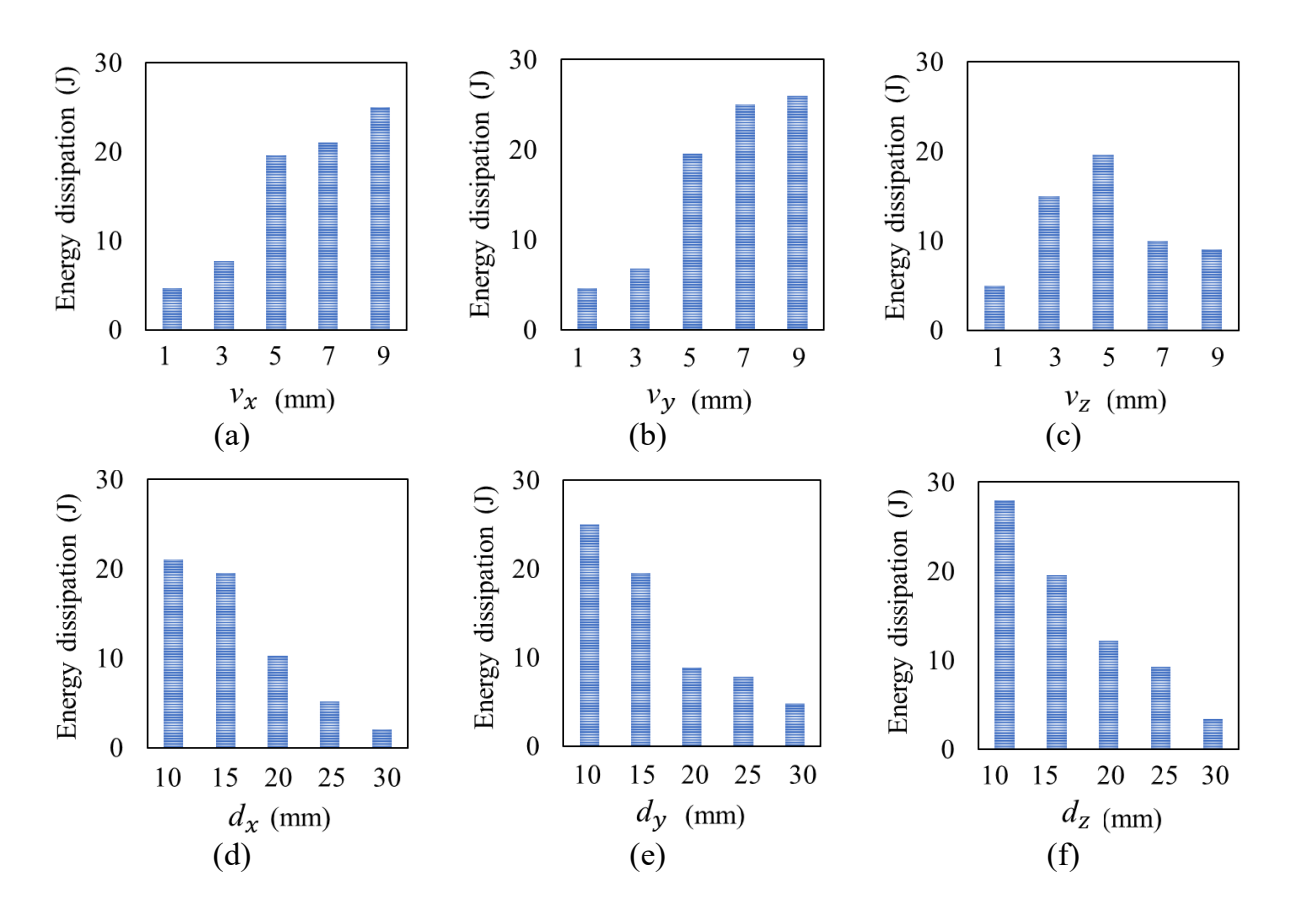


Fig. 15. Propagation and arrestment of cracks in (a) plain concrete, and (b) APCC beam.

The presence of polymer filaments and the occurrence of interfacial debonding between polymer filaments and concrete enhance the energy dissipation capability of APCC beams. The effect of the design variables of APCC on the energy dissipation of APCC beams is shown in **Fig. 16**. The results show that increasing  $v_x$  and  $v_y$  increases the energy dissipation; decreasing  $d_x$ ,  $d_y$  and  $d_z$  increases the energy dissipation; and increase  $v_z$  first increases and then decreases the energy dissipation.



**Fig. 16.** Effect of the design variables of APCC on the energy dissipation: (a)  $v_x$ , (b)  $v_y$ , (c)  $v_z$ , (d)  $d_x$ , (e)  $d_y$ , (f) and  $d_z$ .

## 3.3. Variable importance

The effect of the design variables on  $\delta$  and  $\beta$  is shown in Fig. 17. The lower and upper limits of a box show the first quartile  $(Q_1)$  and third quartile  $(Q_3)$ . The minimum and maximum values of  $\delta$  and  $\beta$  for each variable are represented by the vertical lines of each box. The mean values of  $\delta$  and  $\beta$  for each design variable are shown by symbol "×". The interquartile range (IQR) is the center of a dataset and shown by the box height. The IQR is the difference between the lower quartile  $(Q_1)$  and the upper quartile  $(Q_3)$ . The interquartile ranges of the box and whisker plot of  $\delta$  and  $\beta$  are elaborated in Table 8. According to the table,  $v_x$  and  $v_y$  have comparable effects on  $\delta$  and  $\beta$  since they have comparable lengths of the box and whisker plot. Along Z direction, the effect of adjacent filament spacing is greater

than the effect of filament dimensions on the flexural properties. Decreasing the spacing between adjacent filaments along Z direction increases  $\delta$  and  $\beta$ . The results show that  $d_z$  has the highest effect on  $\delta$  and  $\beta$ , with lengths of 2.49 and 13.70, respectively, due to the higher interquartile range compared with the other design variables.

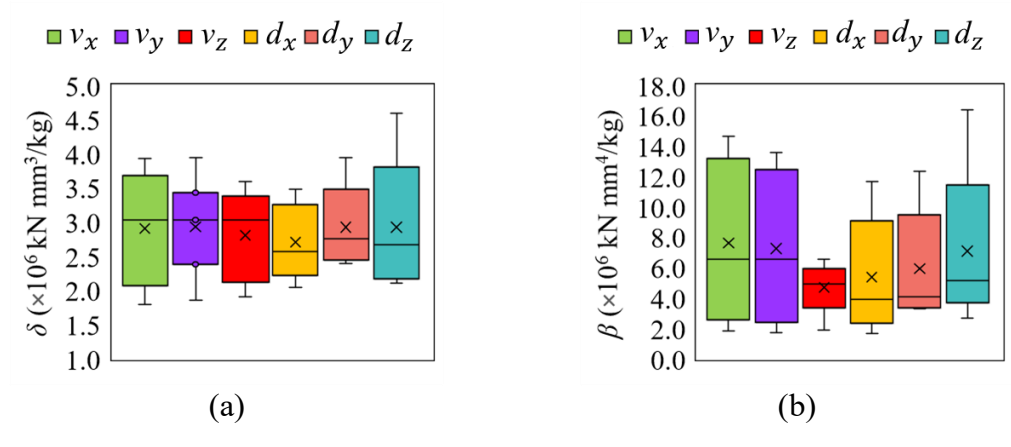


Fig. 17. Box and whisker plot of (a) specific strength ( $\delta$ ), and (b) specific toughness ( $\beta$ ), by  $v_x, v_y, v_z, d_x, d_y$ , and  $d_z$ .

**Table 9.** Interquartile range of the box and whisker plot

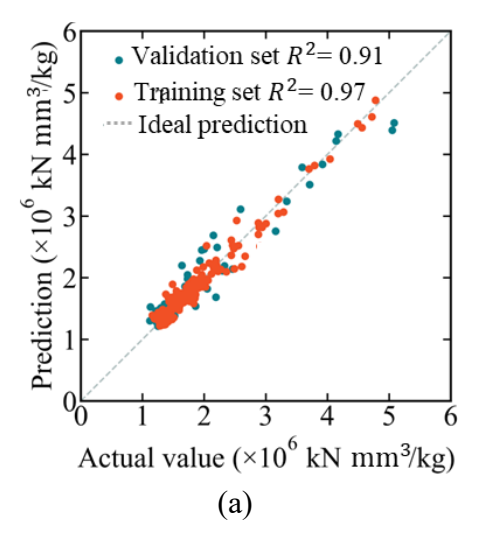
δ						β				
Designation		$(\times 10^6 \text{ kN})$	mm <sup>3</sup> /kg)			$(\times 10^6 \text{ kN mm}^4/\text{kg})$				
-	$Q_1$	$Q_2$	$Q_3$	Range	$Q_1$	$Q_2$	$Q_3$	Range		
$v_x$	1.79	2.91	3.93	2.14	1.88	7.63	14.70	12.82		
$v_{\mathcal{Y}}$	1.87	2.93	3.95	2.08	1.74	7.29	13.60	11.86		
$v_z$	1.91	2.81	3.60	1.69	1.89	4.73	6.59	4.70		
$d_{x}$	2.05	2.71	3.49	1.44	1.66	5.38	11.70	10.04		
$d_{y}$	2.40	2.93	3.95	1.55	3.30	5.96	12.40	9.10		
$\underline{}$	2.11	2.93	4.60	2.49	2.70	7.11	16.40	13.70		

# 4. Design Optimization

## 4.1. Prediction results

The sequential surrogate model was used to predict the specific flexural strength of APCC. To train the predictive model, initial datasets were generated using the finite element model for training and validation. More samples were sequentially added to the training dataset to improve the accuracy of the model. In this study, an initial dataset was established using the results from

10 finite element models. Another 60 finite element models were established to generate new samples to enlarge the training dataset. The prediction results are compared with the finite element analysis results, as shown in **Fig. 18**. The actual results were obtained from the finite element model, and the prediction results were obtained from the sequential surrogate model and automated machine learning [51], which automates the tuning of sequential surrogate models.



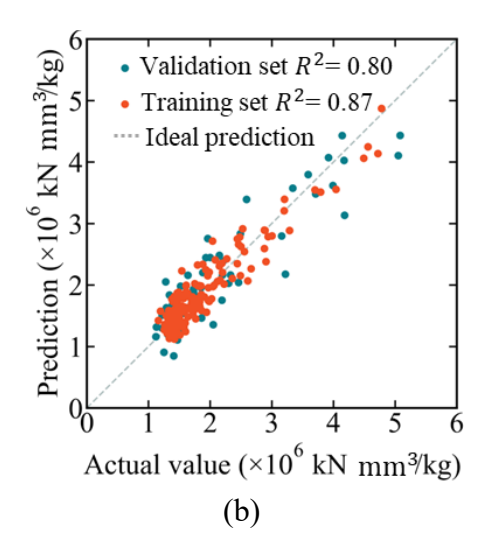


**Fig. 18.** Comparison of the prediction and actual results of the specific flexural strength: (a) sequential surrogate model, and (b) automated machine learning model.

The performance metrics of the training and validation datasets are shown in **Table 10**. The  $R^2$  value of training set using the sequential surrogate model decreases from 0.87 to 0.97, and the  $R^2$  value of validation set using the sequential surrogate model decreases from 0.80 to 0.91. Such an improvement reveals the high performance of the sequential surrogate model which enhances the performance of a prediction model based on the same dataset. The results show that the sequential surrogate model can reasonably predict the mechanical properties of the APCC.

**Table 10.** Performance metrics of the machine learning models

Dataset	Performance metrics -	Specific flexural streng	th (×10 <sup>6</sup> kN mm <sup>3</sup> /kg)
Dataset	remonificance metrics -	Automated machine learning	Sequential surrogate model
Torinin	$R^2$	0.87	0.97
Training	RMSE	0.16	0.06
Validation	$R^2$	0.80	0.91
Validation	RMSE	0.20	0.12

# 4.2. Optimization results

The results of the optimal design and initial design of APCC are listed in **Table 11**. The specific flexural strength and specific toughness of the optimal design are increased by 197% and 234%, respectively, compared with the initial design.

**Table 11.** Comparison between initial and optimal design

Designation	Dimension (mm)						δ	β	Improvement (%)		
8	$v_x$	$v_y$	$v_z$	$d_{x}$	$d_y$	$d_z$	$(\times 10^6 \text{ kN mm}^3/\text{kg})$	(×10° KN mm <sup>-7</sup> /kg)	δ	β	
Initial	5	5	5	15	15	15	3.03	6.59	197%	234%	
Optimal	9	9	9	15	15	15	9.04	22.0	19/70	23470	

The flexural properties of APCC beams made using the optimal design, the initial design, and plain concrete are compared in **Fig. 19**. The finite element analysis results agree with the experimental results. Compared with plain concrete, the optimal design of APCC increases the specific flexural strength, specific toughness, and energy dissipation by 230%, 2245%, and 2841%, respectively.

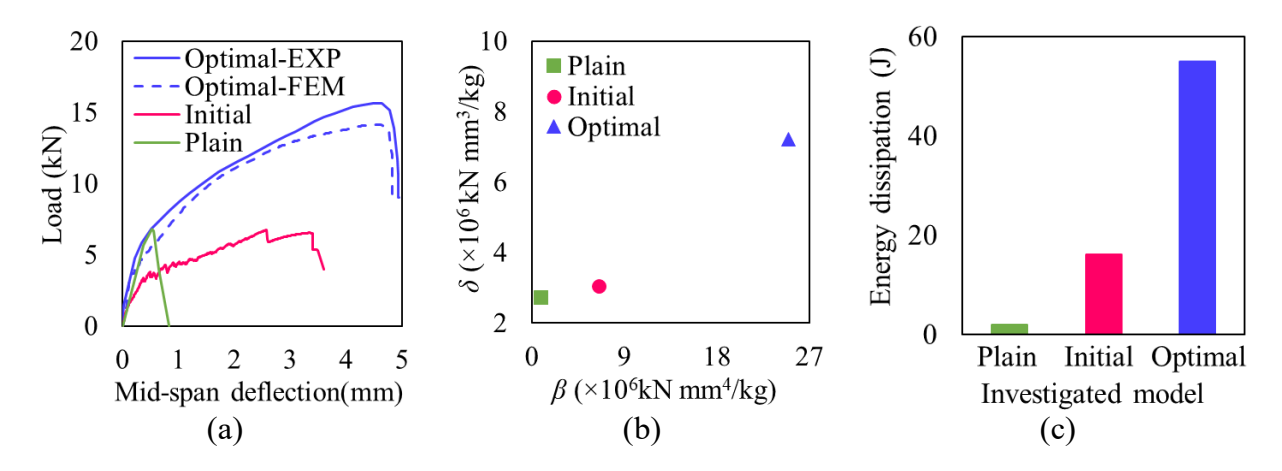


**Fig. 19.** Finite element analysis results of APCC beams made using the optimal design, initial design, and plain concrete: (a) load-deflection curve, (b) specific flexural strength and specific toughness, and (c) energy dissipation.

Fig. 20 shows the energy dissipation history of concrete and polymer lattices in the loading process. Before concrete is cracked, concrete matrix absorbs more energy than polymer lattices since the volume of concrete is larger than that of polymer lattices. After concrete is cracked, polymer lattices absorb more energy since ABS has a higher tensile strength than concrete.

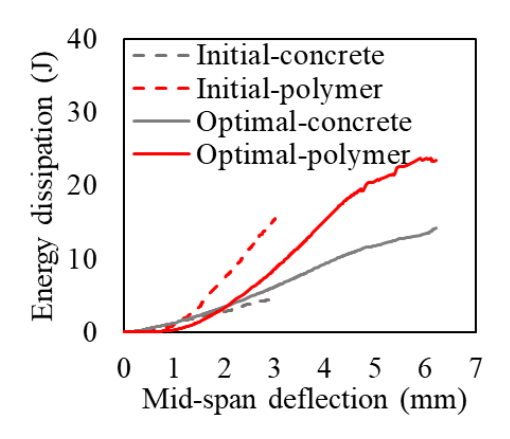


Fig. 20. Energy dissipation in concrete and polymer sections of initial and optimal design.

#### 5. Conclusions

This study proposes a machine learning-based optimization framework to design APCC, aiming to achieve high specific flexural strength and high specific toughness. Based on the above investigations, the following conclusions are drawn:

- The proposed optimization framework is effective in designing APCC with high specific flexural strength and high specific toughness as well as 3D printability. Compared with the beam made of plain concrete, the beam with the optimal design of APCC increased the specific flexural strength, specific toughness, and energy dissipation by 230%, 2245%, and 2841%, respectively. The APCC beams achieved strain-hardening properties and exhibited multiple cracks which increased the deformability.
- The underlying mechanisms of enhancing the flexural properties by polymer lattices were investigated. The flexural strength is increased through the bridging effect of polymer lattices that hinder the widening of cracks due to the high tensile strength of the polymer.

The toughness is increased by the increase of the flexural strength and ductility of APCC. The ductility is increased by multiple mechanisms. First, the presence of polymer lattices reduces the area of concrete periodically, promoting the generation of multiple cracks. Second, the polymer lattices hinder the fracture failure of APCC by bridging the cracks. Third, the presence of polymer lattices promotes the occurrence of horizontal cracks. An interesting and important finding is that the polymer lattices do not hinder the initiation of cracks. Instead, they promote the initiation of cracks, but they control the propagation of cracks. Catastrophic propagation of vertical cracks is hindered, and horizontal cracks are promoted. In summary, the use of polymer lattices imparts various mechanisms to hinder failure and dissipate energy.

• The parametric study uncovered the effect of the design variables of polymer lattices on the specific flexural strength and specific toughness of APCC. The quantification of the effect of design variables promotes the design and optimization of APCC. This study used a metaheuristic optimization algorithm to efficiently search the optimal solution.

This research is limited to the design, fabrication, and testing of small-scale beams with ABS lattices embedded in concrete mortar. Further research is necessary to understand the performance of the proposed methods in large-scale applications. It is envisioned that the methods can be up-scaled since the 3D printed polymer lattices can be assembled to generate large-scale polymer lattices for various structural components. It is also interesting to test the performance of other types of polymer and cement-based materials.

## Acknowledgement

This research was funded by the National Science Foundation of the United States [award number: CMMI-2046407].

#### 461 **References**

- [1] Kelly, T., Matos, G.R., Buckingham, D.A., DiFrancesco, C.A., Porter, K.E., Berry, C., Crane,
- M., Goonan, T. and Sznopek, J., 2005. Historical statistics for mineral and material
- 464 commodities in the United States. US Geological Survey. <a href="https://doi.org/10.3133/ds140">https://doi.org/10.3133/ds140</a>
- 465 [2] Moya, Q., & Pons, O., 2014. Improving the design and production data flow of a complex
- 466 curvilinear geometric Glass Reinforced Concrete façade. Automation in construction, 38,
- 467 pp.46-58. https://doi.org/10.1016/j.autcon.2013.10.025
- 468 [3] Kang, F., Liu, J., Li, J. and Li, S., 2017. Concrete dam deformation prediction model for
- health monitoring based on extreme learning machine. Structural Control and Health
- 470 Monitoring, 24(10), p.e1997. https://doi.org/10.1002/stc.1997
- 471 [4] Chen, D., Sun, G., Meng, M., Jin, X., Li, Q., 2019. Flexural performance and cost efficiency
- of carbon/basalt/glass hybrid FRP composite laminates. Thin-Walled Structures, 142,
- 473 pp.516-531. https://doi.org/10.1016/j.tws.2019.03.056
- 474 [5] Fan, L., Meng, W., Teng, L. and Khayat, K.H., 2019. Effect of steel fibers with galvanized
- coatings on corrosion of steel bars embedded in UHPC. Composites Part B: Engineering,
- 476 177, p.107445. https://doi.org/10.1016/j.compositesb.2019.107445
- 477 [6] Fan, L., Bao, Y., Meng, W. and Chen, G., 2019. In-situ monitoring of corrosion-induced
- 478 expansion and mass loss of steel bar in steel fiber reinforced concrete using a distributed
- fiber optic sensor. Composites Part B: Engineering, 165, pp.679-689.
- 480 https://doi.org/10.1016/j.compositesb.2019.02.051
- 481 [7] Nguyễn, H.H., Nguyễn, P.H., Lương, Q.H., Meng, W. and Lee, B.Y., 2023. Mechanical and
- autogenous healing properties of high-strength and ultra-ductility engineered geopolymer
- 483 composites reinforced by PE-PVA hybrid fibers. Cement and Concrete Composites, 142,

- 484 p.105155. https://doi.org/10.1016/j.cemconcomp.2023.105155
- [8] Zeng, Y., Zhou, X., Tang, A., Sun, P., 2020. Mechanical properties of chopped basalt fiber-
- 486 reinforced lightweight aggregate concrete and chopped polyacrylonitrile fiber reinforced
- lightweight aggregate concrete. Materials, 13(7), p.1715.
- 488 <u>https://doi.org/10.3390/ma13071715</u>
- 489 [9] Du, J., Meng, W., Khayat, K. H., Bao, Y., Guo, P., Lyu, Z., Abu-obeidah, A., Nassif, H.,
- Wang, H., 2021. New development of ultra-high-performance concrete (UHPC).
- 491 Composites Part B: Engineering, 224, p.109220.
- 492 https://doi.org/10.1016/j.compositesb.2021.109220
- 493 [10] Li, V.C., 2003. On engineered cementitious composites (ECC) a review of the material and
- its applications. Journal of Advanced Concrete Technology, 1 (3), pp.215-230.
- 495 https://doi.org/10.3151/jact.1.215
- 496 [11] Zhou, Y., Gong, G., Xi, B., Guo, M., Xing, F. and Chen, C., 2022. Sustainable lightweight
- 497 engineered cementitious composites using limestone calcined clay cement (LC3).
- 498 Composites Part B: Engineering, 243, p.110183.
- 499 <u>https://doi.org/10.1016/j.compositesb.2022.110183</u>
- 500 [12] Meng, W. and Khayat, K.H., 2016. Mechanical properties of ultra-high-performance
- concrete enhanced with graphite nanoplatelets and carbon nanofibers. Composites Part B:
- Engineering, 107, pp.113-122. <a href="https://doi.org/10.1016/j.compositesb.2016.09.069">https://doi.org/10.1016/j.compositesb.2016.09.069</a>
- 503 [13] Meng, W., Valipour, M. and Khayat, K.H., 2017. Optimization and performance of cost-
- effective ultra-high performance concrete. Materials and structures, 50, pp.1-16.
- 505 https://link.springer.com/article/10.1617/s11527-016-0896-3
- 506 [14] Meng, W. and Khayat, K.H., 2017. Improving flexural performance of ultra-high-

- 507 performance concrete by rheology control of suspending mortar. Composites Part B:
- 508 Engineering, 117, pp.26-34. https://doi.org/10.1016/j.compositesb.2017.02.019
- 509 [15] Teng, L., Meng, W. and Khayat, K.H., 2020. Rheology control of ultra-high-performance
- concrete made with different fiber contents. Cement and Concrete Research, 138, p.106222.
- 511 https://doi.org/10.1016/j.cemconres.2020.106222
- 512 [16] Iqbal, S., Ali, A., Holschemacher, K. and Bier, T.A., 2015. Mechanical properties of steel
- 513 fiber reinforced high strength lightweight self-compacting concrete (SHLSCC).
- 514 Construction and Building Materials, 98, pp.325-333.
- 515 https://doi.org/10.1016/j.conbuildmat.2015.08.112
- 516 [17] Liu, Y., Zhang, Z., Shi, C., Zhu, D., Li, N. and Deng, Y., 2020. Development of ultra-high
- performance geopolymer concrete (UHPGC): Influence of steel fiber on mechanical
- properties. Cement and Concrete Composites, 112, p.103670.
- 519 https://doi.org/10.1016/j.cemconcomp.2020.103670
- 520 [18] Mudadu, A., Tiberti, G., Germano, F., Plizzari, G. A., Morbi, A., 2018. The effect of fiber
- orientation on the post-cracking behavior of steel fiber reinforced concrete under bending
- and uniaxial tensile tests. Cement and Concrete Composites, 93, pp.274-288.
- 523 <u>https://doi.org/10.1016/j.cemconcomp.2018.07.012</u>
- 524 [19] Xue, Y., Wang, W. and Han, F., 2019. Enhanced compressive mechanical properties of
- aluminum based auxetic lattice structures filled with polymers. Composites Part B:
- Engineering, 171, pp.183-191. https://doi.org/10.1016/j.compositesb.2019.05.002
- 527 [20] Xu, W., Jambhulkar, S., Zhu, Y., Ravichandran, D., Kakarla, M., Vernon, B., Lott, D.G.,
- 528 Cornella, J.L., Shefi, O., Miquelard-Garnier, G. and Yang, Y., 2021. 3D printing for
- polymer/particle-based processing: A review. Composites Part B: Engineering, 223,

- p.109102. <a href="https://doi.org/10.1016/j.compositesb.2021.109102">https://doi.org/10.1016/j.compositesb.2021.109102</a>
- 531 [21] Zhang, X.G., Ren, X., Jiang, W., Zhang, X.Y., Luo, C., Zhang, Y. and Xie, Y.M., 2022. A
- novel auxetic chiral lattice composite: Experimental and numerical study. Composite
- 533 Structures, 282, p.115043. https://doi.org/10.1016/j.compstruct.2021.115043
- 534 [22] Luo, H.C., Ren, X., Zhang, Y., Zhang, X.Y., Zhang, X.G., Luo, C., Cheng, X. and Xie,
- Y.M., 2022. Mechanical properties of foam-filled hexagonal and re-entrant honeycombs
- under uniaxial compression. Composite Structures, 280, p.114922.
- 537 https://doi.org/10.1016/j.compstruct.2021.114922
- 538 [23] Guo, X., Ding, J., Li, X., Qu, S., Fuh, J.Y.H., Lu, W.F., Song, X. and Zhai, W., 2023.
- Interpenetrating phase composites with 3D printed triply periodic minimal surface (TPMS)
- lattice structures. Composites Part B: Engineering, 248, p.110351.
- 541 https://doi.org/10.1016/j.cemconcomp.2023.105046
- 542 [24] Salazar, B., Aghdasi, P., Williams, I., Ostertag, C., Taylor, H., 2020. Polymer lattice-
- reinforcement for enhancing ductility of concrete. Materials & Design, 196, p.109184.
- 544 <u>https://doi.org/10.1016/j.matdes.2020.109184</u>
- 545 [25] Xu, Y., Šavija, B., 2019. Development of strain hardening cementitious composite (SHCC)
- reinforced with 3D printed polymeric reinforcement: Mechanical properties. Composites
- Part B: Engineering, 174, p.107011. <a href="https://doi.org/10.1016/j.compositesb.2019.107011">https://doi.org/10.1016/j.compositesb.2019.107011</a>
- 548 [26] Zhou, H., Jia, K., Wang, X., Xiong, M.X. and Wang, Y., 2020. Experimental and numerical
- investigation of low velocity impact response of foam concrete filled auxetic honeycombs.
- Thin-Walled Structures, 154, p.106898. <a href="https://doi.org/10.1016/j.tws.2020.106898">https://doi.org/10.1016/j.tws.2020.106898</a>
- 551 [27] Tzortzinis, G., Gross, A. and Gerasimidis, S., 2022. Auxetic boosting of confinement in
- mortar by 3D reentrant truss lattices for next generation steel reinforced concrete members.

- Extreme Mechanics Letters, 52, p.101681. <a href="https://doi.org/10.1016/j.eml.2022.101681">https://doi.org/10.1016/j.eml.2022.101681</a>
- 554 [28] Zhong, R., Ren, X., Zhang, X.Y., Luo, C., Zhang, Y. and Xie, Y.M., 2022. Mechanical
- properties of concrete composites with auxetic single and layered honeycomb structures.
- 556 Construction and Building Materials, 322, p.126453.
- 557 https://doi.org/10.1016/j.conbuildmat.2022.126453
- 558 [29] Chen, M., Chen, Z., Xuan, Y., Zhang, T. and Zhang, M., 2023. Static and dynamic
- compressive behaviour of 3D printed auxetic lattice reinforced ultra-high performance
- 560 concrete. Cement and Concrete Composites, 139, p.105046.
- 561 https://doi.org/10.1016/j.cemconcomp.2023.105046
- 562 [30] ABAQUS/CAE Version 2017. Software for Technical Computation. Simulia Corp:
- Providence, RI, United States, 2017. <a href="https://www.3ds.com/products-">https://www.3ds.com/products-</a>
- services/simulia/products/abaqus/abaquscae/
- 565 [31] Mckay, M.D., Beckman, R.J., Conover, W. J., 2000. Comparison of three methods for
- selecting values of input variables in the analysis of output from a computer code.
- 567 Technometrics, 42 (1), pp.55-61.
- 568 <u>https://www.tandfonline.com/doi/abs/10.1080/00401706.2000.10485979</u>
- 569 [32] Jin, S.-S., Jung, H.-J., 2016. Sequential surrogate modeling for efficient finite element
- 570 model updating. Computers & Structures, 168, pp.30-45.
- 571 <u>https://doi.org/10.1016/j.compstruc.2016.02.005</u>
- 572 [33] Kaveh, A., Mahjoubi, S., 2018. Lion pride optimization algorithm: a meta-heuristic method
- for global optimization problems. Scientia Iranica, 25, pp.3113-3132.
- 574 10.24200/SCI.2018.20833
- 575 [34] Nagesha, B. K., Dhinakaran, V., Shree, M.V., Kumar, K. P. M., Chalawadi, D., Sathish, T.,

- 576 2020. Review of characterization and impacts of the lattice structure in additive
- 577 manufacturing. Materials Today: Proceedings, 21, pp.916-919.
- 578 https://doi.org/10.1016/j.matpr.2019.08.158
- 579 [35] Iman, R.L., Helton, J.C., Campbell, J.E., 2018. An approach to sensitivity analysis of
- computer models: Part I—Introduction, input variable selection and preliminary variable
- assessment. Journal of Quality Technology, 13(3), pp.174-183.
- 582 https://doi.org/10.1080/00224065.1981.11978748
- 583 [36] Loeppky, J.L., Sacks, J., Welch, W.J., 2009. Choosing the sample size of a computer
- experiment: A practical guide. Technometrics, 51(4), pp.366-376.
- 585 https://doi.org/10.1198/TECH.2009.08040
- 586 [37] Eason, J., Cremaschi, S., 2014. Adaptive sequential sampling for surrogate model
- generation with artificial neural networks. Computers & Chemical Engineering, 68, pp.220-
- 588 232. https://doi.org/10.1016/j.compchemeng.2014.05.021
- [38] Jones, D. R., 2001. A taxonomy of global optimization methods based on response surfaces.
- Journal of global optimization, 21, pp.345-383. https://doi.org/10.1023/A:1012771025575
- 591 [39] Forrester, A. I. J., Sobester, A., Keane, A. J., 2008. Engineering design via surrogate
- modelling: a practical guide. John Wiley & Sons. <u>10.1002/9780470770801</u>
- 593 [40] Santner, T. J., Williams, B. J., Notz, W. I., Williams, B. J., 2003. The design and analysis of
- 594 computer experiments. New York: Springer. <a href="https://www.asc.ohio-state.edu/santner.1/TJS-">https://www.asc.ohio-state.edu/santner.1/TJS-</a>
- 595 BJW-WIN/master-driver.pdf
- 596 [41] Barhemat, R., Mahjoubi, S., Li, V. C., Bao, Y., 2022. Lego-inspired reconfigurable modular
- 597 blocks for automated construction of engineering structures. Automation in Construction,
- 598 139, p.104323, https://doi.org/10.1016/j.autcon.2022.104323

- 599 [42] Kaveh, A., Mahjoubi, S., 2019. Hypotrochoid spiral optimization approach for sizing and
- layout optimization of truss structures with multiple frequency constraints. Engineering with
- 601 Computers, 35, pp.1443-1462. <a href="https://doi.org/10.1007/s00366-018-0675-6">https://doi.org/10.1007/s00366-018-0675-6</a>
- 602 [43] Boparai, K.S., Singh, R., Singh, H., 2016. Development of rapid tooling using fused
- deposition modeling: a review. Rapid Prototyping Journal, 22 (2), pp.281-299.
- 604 https://doi.org/10.1108/RPJ-04-2014-0048
- 605 [44] ASTM C109 / C109M 20b., 2020. Standard Test Method for Compressive Strength of
- Hydraulic Cement Mortars (using 2-in. or [50-mm] Cube Specimens). ASTM International,
- United States. https://www.astm.org/c0109 c0109m-20.html
- 608 [45] ACI, 2019. Building code requirements for structural concrete (ACI 318-19) and
- commentary. <a href="https://www.concrete.org/news/newsdetail.aspx?f=51719135">https://www.concrete.org/news/newsdetail.aspx?f=51719135</a>
- [46] Sümer, Y. and Aktaş, M., 2015. Defining parameters for concrete damage plasticity model.
- 611 Challenge Journal of Structural Mechanics, 1(3), pp.149-155.
- https://doi.org/10.20528/cjsmec.2015.07.023
- 613 [47] Hafezolghorani, M., Hejazi, F., Vaghei, R., Jaafar, M.S.B. and Karimzade, K., 2017.
- Simplified damage plasticity model for concrete. Structural Engineering International,
- 615 27(1), pp.68-78. https://doi.org/10.2749/101686616X1081
- 616 [48] Neve, S., Du, J., Barhemat, R., Meng, W., Bao, Y., Sarkar, D., 2023. Valorization of vetiver
- root biochar in eco-friendly reinforced concrete: Mechanical, economic, and environmental
- performance. Materials, 16(6), p.2522. https://doi.org/10.3390/ma16062522
- 619 [49] Fadeel, A., Mian, A., Al Rifaie, M., Srinivasan, R., 2019. Effect of vertical strut
- arrangements on compression characteristics of 3D printed polymer lattice structures:
- Experimental and computational study. Journal of Materials Engineering and Performance,

622	28, pp.709-716. https://doi.org/10.1007/s11665-018-3810-z					
623	[50] Tan, X., Mahjoubi, S., Zou, X., Meng, W., Bao, Y., 2023. Metaheuristic inverse analysis on					
624	interfacial mechanics of distributed fiber optic sensors undergoing interfacial debonding.					
625	Mechanical S	ystems a	nd Signal	Processing,	200,	p.110532.
626	https://doi.org/10.1016/j.ymssp.2023.110532					
627	[51] Copeland, M., Soh, J., Puca, A., Manning, M., Gollob, D., 2015. Microsoft Azure and cloud					
628	computing, Microsoft Azure, pp.3-26. <a href="https://doi.org/10.1007/978-1-4842-1043-7_1">https://doi.org/10.1007/978-1-4842-1043-7_1</a>					